01 Jan 2023

Real-Time Air Gap And Thickness Measurement Of Continuous Caster Mold Flux By Extrinsic Fabry-Perot Interferometer

Abhishek Prakash Hungund

Hanok Tekle

Bohong Zhang

Ronald J. O'Malley
Missouri University of Science and Technology, omalleyr@mst.edu

et. al. For a complete list of authors, see https://scholarsmine.mst.edu/matsci_eng_facwork/3269

Recommended Citation

A. P. Hungund et al., "Real-Time Air Gap And Thickness Measurement Of Continuous Caster Mold Flux By Extrinsic Fabry-Perot Interferometer," *IEEE Transactions on Instrumentation and Measurement*, Institute of Electrical and Electronics Engineers, Jan 2023.
The definitive version is available at https://doi.org/10.1109/TIM.2023.3326240

Real-Time Air Gap and Thickness Measurement of Continuous Caster Mold Flux by Extrinsic Fabry–Perot Interferometer

Abhishek Prakash Hungund, Hanok Tekle, Bohong Zhang, *Member, IEEE*, Ronald J. O'Malley, Jeffrey D. Smith, Rex E. Gerald, II, and Jie Huang, *Senior Member, IEEE*

***Abstract*— Mold Flux plays a critical role in the continuous casting of steel. Along with many other functions, the mold flux in the gap between the solidifying steel shell and the mold serves as a medium for controlling heat transfer and as a barrier to prevent the shell from sticking to the mold. This manuscript introduces a novel method of monitoring the structural features of a mold flux film in real time in a simulated mold gap. A three-part stainless-steel mold was designed with a 2, 4, and 6 mm step profile to contain mold flux films of varying thickness. An extrinsic Fabry–Perot interferometer (EFPI) was installed at each of the three steps in the mold. Mold flux was melted in a graphite crucible at 1400 °C and poured into the instrumented step mold for analysis. Interferograms from the three EFPIs were acquired and processed in real time to measure the air gap and thickness of each flux film during solidification. Measurements were performed on two different mold flux compositions. Results demonstrate that the proposed system successfully records structural features of the flux film in real time during cooling. It has a large real-time impact on the process control of steel making and optimizing the quality of steel castings. In addition, the measurement method has the potential to monitor crystal nucleation and growth in a variety of crystallizing glass systems.**

***Index Terms*— Air gap, basicity, extrinsic Fabry–Perot interferometer (EFPI), interferogram, mold flux, real-time measurement, single-mode fiber (SMF), thickness measurement.**

I. Introduction

MOLD flux is an engineered calcium silicon oxyfluoride glass that is designed with a target viscosity and crystallization behavior for use as a lubricant in the continuous casting process. Mold flux is often spray dried and carbon coated to control its melting behavior in the mold [1], and a liquid layer of the flux develops on the steel surface and then enters the mold gap around the mold perimeter. Mold flux has several functions, such as protection of molten steel from oxidation [2], heat removal control during initial steel shell formation [3], absorption of nonmetallic inclusions [4], lubrication of the solidifying steel strands during extraction, and thermal insulation [5]. If the mold flux has a high degree of crystallinity, the steel shell that exits the mold can be excessively thin, leading to shell bulging due to the shell's inability to withstand the ferrostatic pressure of the internal molten steel [6]; furthermore, during the casting process, mold flux aids in the absorption of nonmetallic inclusions in steel [7], and as such, the flux can experience composition changes that affect flux viscosity and crystallization behavior. Studying the structural properties of mold flux in mold gap can provide new insights into the prevailing flux film heat transfer, mold interface contact resistance, and their links to crystallization behavior. An efficient way of measuring air gap and flux film thickness for several continuous casting mold fluxes during cooling and solidification is presented in this research.

Crystallization is defined as the process by which a liquid or short-range order glass transforms to an ordered crystal structure, such that the overall energy of the system is minimized [8], [9], [10]. Nucleation occurs at the onset of crystallization when the atoms or molecules of molten flux arrange themselves to form crystals of a critical size to support thermodynamically stable growth [11]. The nucleation rate is important in determining crystalline structure and grain size [12] in the flux film. In the continuous casting process, the liquid flux enters the mold gap at the mold perimeter, and the portion of the flux that contacts the mold is rapidly cooled to form a glass. The molten flux undergoes a wide range of cooling conditions under which crystallization is promoted, and crystal nuclei will form and grow. While the flux nearest to the hot steel remains liquid, other parts of the flux film exhibit a range of cooling conditions that can either promote direct crystal formation from the liquid or crystallization from the glass. This process is difficult to study, making EFPI a great candidate for the proposed sensor solution [13]. The flux also undergoes thermal contraction as it cools, which results in shrinkage [14]. Shrinkage can cause the flux to pull away

Manuscript received 28 June 2023; revised 18 September 2023; accepted 8 October 2023. Date of publication 20 October 2023; date of current version 2 November 2023. This work was supported in part by the DLA-Troop Support, Philadelphia, PA, USA; in part by the Defense Logistics Agency Information Operations, J68, Research and Development, Ft. Belvoir, VA, USA; in part by the Department of Energy's Office of Energy Efficiency and Renewable Energy (EERE) through the Advanced Manufacturing Office (AMO) under Award DE-EE0009119; and in part by the Peaslee Steel Manufacturing Research Center (PSMRC), Missouri University of Science and Technology, Rolla, MO, USA. The Associate Editor coordinating the review process was Dr. Yuya Koyama. *(Abhishek Prakash Hungund and Hanok Tekle contributed equally to this work.) (Corresponding author: Jie Huang.)*

Abhishek Prakash Hungund, Bohong Zhang, Rex E. Gerald, II, and Jie Huang are with the Department of Electrical and Computer Engineering, Missouri University of Science and Technology, Rolla, MO 65409 USA (e-mail: jieh@mst.edu).

Hanok Tekle, Ronald J. O'Malley, and Jeffrey D. Smith are with the Department of Materials and Science Engineering, Missouri University of Science and Technology, Rolla, MO 65409 USA (e-mail: omalleyr@mst.edu).

Digital Object Identifier 10.1109/TIM.2023.3326240

from the mold wall, increasing resistance to heat flow at the interface. Cracks can also form in the flux film as it contracts if the surface of the mold becomes too rigid to accommodate internal shrinkage [15]. The overall flux film thickness and the thickness of the air gap between the flux film and the mold wall are a consequence of this shrinkage.

Several methods have been used in heat transfer simulations of the continuous casting mold to predict or calculate the flux film air gap and thickness during molten flux solidification [16], [17]; however, to date, air gap and flux thickness have not been measured in situ during flux solidification, and instead, flux film surface roughness, thickness, and temperature profile measurements across mold gap have been used to estimate these parameters. The mold flux serves several primary functions in the continuous casting of the steel, as discussed earlier. Hence, measurements of the air gap and flux film thickness are relevant because they provide information that directly impacts the quality of steel being manufactured. Mold fluxes exhibit both glassy and crystalline phases during cooling [18]. For this reason, it is important to understand the effects of these structures on interfacial gap development and mold flux film thickness and their relationships to mold heal removal.

In the steel casting industries, various methods have been adopted to measure air gap and slab thickness to enhance the yield and casting quality. Conduction-based sensors provide a direct method for gauging the interfacial heat transfer coefficient (IHTC) by capturing heat transfer, predominantly through conduction, facilitating air gap estimations [19]. The results obtained by this method are only an estimation and may not be accurate. The linear variable differential transformer (LVDT) method and its variants have also been used to measure the air gaps during steel solidification [20]. Another capacitive multipoint electronic probe was reported to measure the air gap between mold and metal during solidification [21]. These types of electronic sensors are susceptible to electromagnetic interference (EMI) and the metal housings of the sensors will expand when they are in proximity to high temperatures, which can result in erroneous measurements.

Fiber-optics are very suitable for highly sensitive measurements [22], [23], [24]. They have several advantages, including electromagnetic immunity, lightweight, flexibility, and compact size [25], [26], [27], [28], [29]. They are also capable of multiplexed and distributed measurement where continuous physical quantity mapping is required, such as temperature and strain [30], [31]. Fiber-optic sensors can detect optical path differences as small as 1 nm when configured as interferometers [32]. In this research, an Extrinsic Fabry–Perot Interferometer (EFPI) is used as a point sensor for air gap measurements. The fiber-optic EFPI system is immune to EMI [33] and can be designed in a highly compact manner [34]. It has high sensitivity making it suitable to detect small changes in the air gap [35]. The EFPI sensors are suitable for high-temperature environments. For example, EFPI sensors made from sapphire fibers can withstand up to 2050 °C [36]. The EFPI sensors that employ silica fibers do not suffer from thermal expansion mismatch [37]. The EFPI sensor can detect reflections from multiple reflective interfaces within a nonopaque material through modulated interferometry [38], which makes it very suitable for the present application.

It is necessary to periodically tune the optical wavelength of the source with a wide wavelength band for mold flux applications. Hence, it is tuned through a relatively large range, such as ∼100 nm, at a sweep rate of 10 or 100 Hz [39]. This cannot be performed using a conventional tunable laser source. A swept laser operates by rapidly changing the instantaneous frequency of the laser output, which is extensively used to interrogate fiber-optic sensors [39], [40] such as in measuring temperature and strain from Fiber Bragg Grating (FBG) sensors [41]. It is also used in EFPI interrogation for acoustics [42] and refractive index [43] sensing.

To summarize, three EFPIs were instrumented and installed in a three-part custom designed mold. The sensors were connected to a wide wavelength band optical interrogator with a swept laser source and an enhanced photodetection module. Data acquisition software was developed in LabVIEW using in-house designed real-time air gap and thickness estimation algorithms. The flux sample was heated and melted in a furnace and then poured into the three-part mold. The measured EFPI signals were used to document and analyze solidification and shrinkage phenomena in two different flux samples.

II. Sensor, Mold Design, and Experimental Setup

A. Sensor Design

Three EFPIs were instrumented in a very simple manner. A single-mode fiber was cleaved and inserted into a stainless-steel ferrule having an outer diameter of 1.25 mm. The hole in the stainless-steel ferrule had an inner diameter of 127 μm, which holds the SMF with a cleaved end face. The fiber end face was not flush with the end of the ferrule. This was done intentionally to have an internal offset such that the point at which molten flux starts to solidify can be clearly detected and to prevent direct contact of molten flux with the fiber end face. Care was taken to ensure that the internal offset did not exceed 200 μm, which would have adversely affected the quality of the measurement. The instrumentation of the EFPI is shown in Fig. 1. The air gap and thickness measurement from the fabricated EFPI sensor are not affected by the thermal expansion of the SMF and stainless-steel ferrule. This is because the SMF expands in a longitudinally opposite direction of the EFPI cavity in such a way that the end face of the fiber, i.e., the first reflector of EFPI, remains in the initial position. The EFPI sensor designed in Fig. 1(a) includes a cleaved SMF inserted into a stainless-steel ferrule with an internal offset for air gap and thickness measurements. The fabrication of the sensor and the setup for measuring the internal offset for gap calibration employing a reflective surface are shown in Fig. 1(b).

Table I shows the offset or the distance by which the cleaved end face of the SMF is inset from the stainless-steel ferrule's hole. Three EFPIs were instrumented, and they were calibrated using a highly reflective magnetic surface for measuring the internal offsets. This is done to prevent penetration of molten flux samples into the sensor. These distances do not interfere with the measurement as they are compensated for

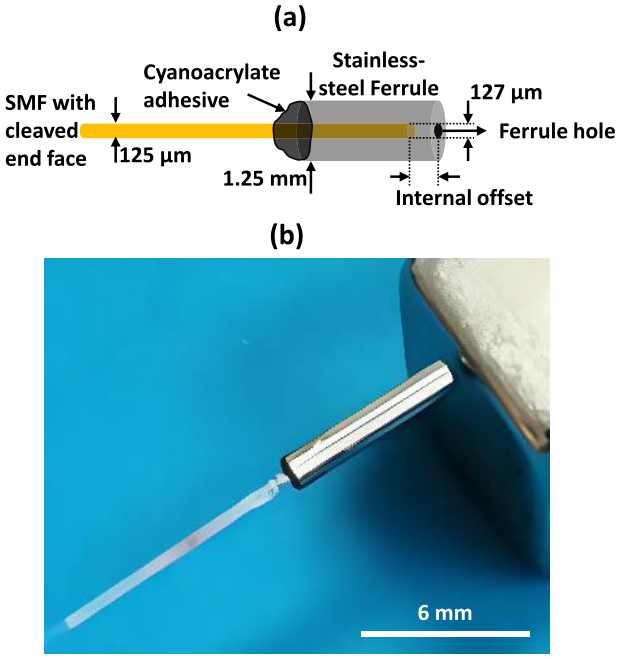

Fig. 1. Instrumentation of EFPI sensor. (a) EFPI sensor design. (b) Photograph of actual fabricated EFPI sensor and gap calibration setup.

TABLE I
EFPI INTERNAL OFFSETS

EFPI Sensor	Internal Offset (µm)
Top	100
Middle	50
Bottom	130

the real-time determination of thickness and air gap. The point gap sensor is a single-mode fiber of 1550BHP–0.13 NA (numerical aperture), having an operating wavelength range of 1460–1620 nm. The fiber had a diameter of 125 μm and was protected by an FT900W polymer tubing.

B. Mold Design and Instrumentation

A three-part mold was designed for the purpose of measuring the air gap and thickness of molten mold flux. For ease of EFPI installation, the mold was designed to have three parts, as shown in Fig. 2. The front plate of the mold was designed to have an opening at the bottom. This allows the molten mold flux sample to flow through the mold with minimal friction and simultaneously have contact with all three-step profiles of the mold.

The front component is a plane wall, which has a smooth finish for good reflection from which light from the EFPIs are reflected. The design and dimensions are shown in Fig. 3(a). The back component of the mold is split into two parts, having step profiles of 2, 4, and 6 mm. The design dimensions are shown in Fig. 3(b) and (c). These two mold parts have grooves in the center such that, when they are joined, they form holes of 1.27 mm inner diameter while retaining the step profile. The holes are used to house and clamp the EFPI ferrules containing the SMF. The EFPIs were installed in the grooves on the left side of the back component with cyanoacrylate adhesive.

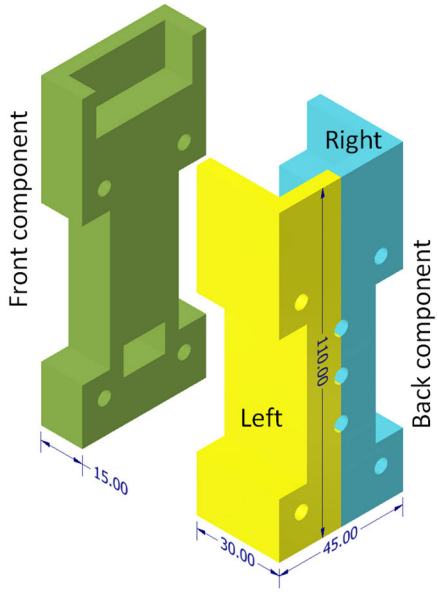

Fig. 2. Mold design and specifications. This figure illustrates the design of a three-part mold used for mold flux analysis. It has a dimension of (110 × 45 × 45) mm when combined.

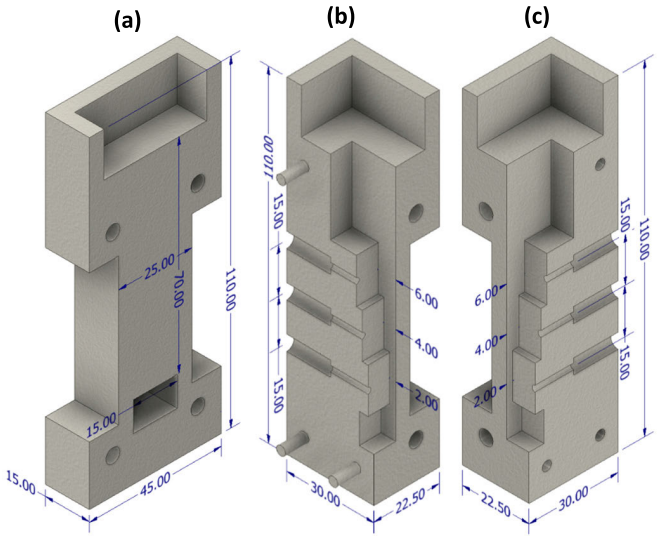

Fig. 3. Three-dimensional model of flux mold with illustrated dimensions. (a) Front component. (b) Left half of back component. (c) Right half of back component.

The back components of the mold and air gap sensors after EFPI installation from which the step profile can be observed in Fig. 4(a). The front component of the mold is bolted to the back components after EFPI installation, such that the wall is facing the sensor, as shown in Fig. 4(b). Fig. 4(c) shows the top view of the mold setup where the synthetic molten flux sample is poured. The SMF cables are shielded with stainless-steel tubing for protection from high temperatures, as shown in Fig. 4(d). The right side of the back component was combined with the opposite half of the mold to provide an enclosure and to affix the ferrules in place. Both parts of the back component were held together with bolts. The front mold component was placed in contact with the back components such that all the EFPIs were exactly perpendicular to the wall.

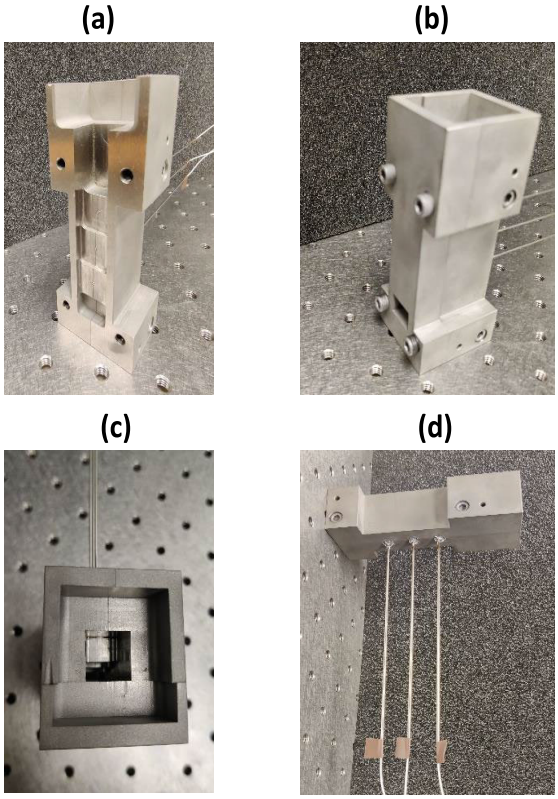

Fig. 4. Flux mold with EFPI sensors installed, including shielding. (a) Back part of the mold with instrumented EFPIs. (b) Complete mold setup–front view. (c) Complete mold setup–top view. (d) Stainless steel tube shielding of the SMF cables.

The fibers extending from the EFPI sensors were protected by a thin stainless-steel tube that protruded from the back of the mold. The mold is shown after the installation of the EFPIs in Fig. 4. The stainless-steel tubes are firmly attached to the back of the mold by means of a high-temperature adhesive, which was cured with a torch. The sensors were then connected to an optical interrogator controlled by a computer.

C. Experimental Setup

The experimental setup shown in Fig. 5 consists of the instrumented mold, optical interrogator, computer to acquire data from the optical interrogator, heating furnace with temperature controller and graphite crucible in which powdered mold flux was poured. First, the instrumented mold was placed on a firm stable platform with the stainless-steel tubes covered by heat resistant material. The single-mode fibers of the three EFPIs were connected to a Micrometer-Optics Hyperion SI-255 enhanced visibility optical interrogator. The Hyperion SI-255 is a 16-channel optical instrument with a swept laser operating at a 10 Hz sweeping rate. It has a very broad wavelength band of 160 nm, from 1460 to 1620 nm.

An empty graphite crucible was preheated to 1400 °C in the furnace. A granular mold flux sample was poured into the graphite crucible and placed in the furnace. The flux sample was then melted at 1400 °C in the furnace. At this point, the data acquisition was initiated on the computer connected to Hyperion SI-255. The graphite crucible with molten flux sample was quickly removed from the furnace and poured into

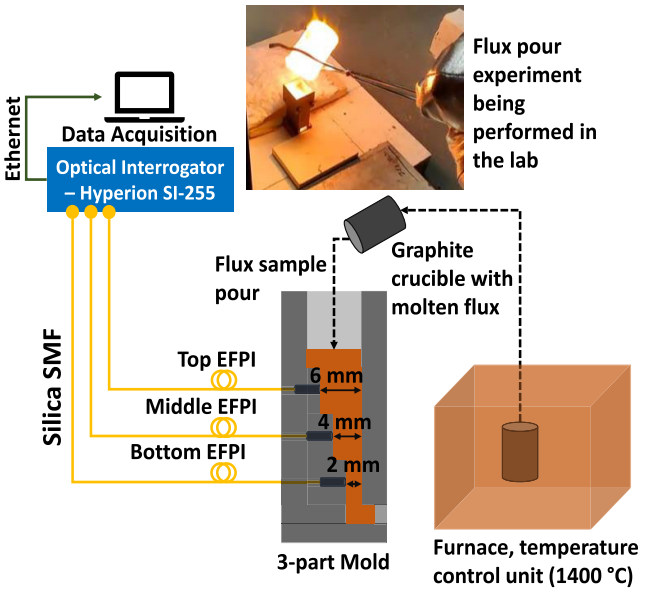

Fig. 5. Experimental setup for measuring air gap and thickness of synthetic mold flux employing real-time acquisition of an optical interferogram.

the instrumented mold. As the sample started to crystallize and solidify, there were multiple cavities formed between the fiber end face inside the stainless-steel ferrule and the interior part of front component of the mold wall, resulting in complex interference pattern. This resulted in an interferogram with varying free spectral range (FSR) measured by the Hyperion SI-255. This spectrum was processed in real time to obtain the structural features of the flux during cooling and solidification of the flux. An FFT of the spectrum was obtained to identify the different cavity reflections in the system.

D. Measurement Theory

As soon as the molten flux was poured into the mold, it started to solidify and shrink. The resulting shrinkage caused an air gap to form between the EFPI sensor and the flux surface facing the EFPI. A second reflection was also sometimes observed from the opposite wall, depending on its distance across the mold cavity and the transparency of the flux film. As flux solidification progresses, several reflectors begin to form within the flux, which can be represented as $R = R_1, R_2, \ldots, R_n$. These reflections are due to the formation of air bubbles, which result from the inadequate mixing, excessive turbulence, and trapped gases within the mold flux in continuous casting. This phenomenon is time and temperature dependent. The measurement was performed for a period of ∼5 min to keep consistency across both samples. Additionally, crystallinity of the mold flux is dependent on its chemistry [44], [45]. Hence, two different flux samples were tested. An example of the multiple reflections that can form during solidification of the mold flux is depicted in Fig. 6. The flux shrinks due to crystallization and solidification resulting in an air gap. Multiple reflectors form within the flux due to entrapment of air bubbles, which facilitate the analysis of the flux material. Reflectors R_2 and R_3 can be used to determine the flux thickness.

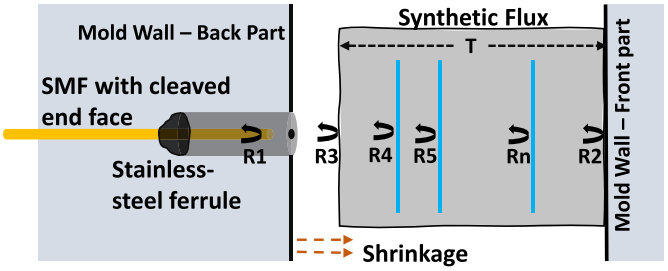

Fig. 6. Measurement of air gap and thickness of flux undergoing crystallization and solidification.

Shrinkage from the back side of the mold is significantly larger than the shrinkage from the front side. This is due to more rapid heat loss from the back of the mold due to the mold wall thickness. Thus, shrinkage from the back of the mold dominates air gap formation. The light intensity reflected from the air gap R_{ag} formed by the cavity due to reflectors (R_1, R_3) is given by

$$R_{ag} = R_1 + R_3 + 2\sqrt{R_1 R_3}\cos\left[\Delta\varphi_{ag} + \varphi_0\right] \tag{1}$$

where φ_{ag} is the phase difference due to the cavity length l_{ag} of the air gap given as follows and φ_0 is the initial phase:

$$\Delta\varphi_{ag} = \frac{4\pi\,\Delta\left(n_a l_{ag}\right)}{\lambda_m} \tag{2}$$

where λ_m is the wavelength of the source and $n_a =\sim 1$ is the refractive index of air. Similarly, the light intensity reflected by the total mold gap with molten flux inside is given by an equation obtained from fast Fourier transform (FFT) analysis of the modulated interferogram

$$R_{mg} = R_1 + R_2 + 2\sqrt{R_1 R_2}\cos\left[\Delta\varphi_{mg} + \varphi_0\right] \tag{3}$$

where R_{mg} is light intensity reflected by the mold gap, as shown in Fig. 6, which is between reflectors (R_1, R_2) and φ_{mg} is the phase difference due to the cavity length l_{mg} between the reflectors (R_1, R_2) given by

$$\Delta\varphi_{mg} = \frac{4\pi\,\Delta\left(n_g l_{mg}\right)}{\lambda_m} \tag{4}$$

where n_g is the group refractive index of the molten mold flux and air gap. The light intensity reflected from the mold flux sample, i.e., between the reflectors (R_3, R_2) can be expressed by the following equation:

$$R_f = R_3 + R_2 + 2\sqrt{R_3 R_2}\cos\left[\Delta\varphi_f + \varphi_0\right] \tag{5}$$

where R_f is light intensity reflected only by the mold flux shown in Fig. 6. The corresponding phase change can be represented by the expression

$$\Delta\varphi_f = \frac{4\pi\,\Delta\left(n_f l_f\right)}{\lambda_m} \tag{6}$$

where φ_f is the phase difference due to the cavity length l_f between the reflectors (R_3, R_2) and $n_f =\sim 1.52$ is the refractive index of the mold flux, which is assumed to be constant throughout. The optical path length $(n_g l_{\text{mg}})$ in (4) is given by

$$n_g l_{mg} = n_a l_{ag} + n_f l_f. \tag{7}$$

The thickness of flux l_f or T can be estimated by rewriting (7) as

$$T = l_f = \frac{n_g l_{mg} - l_{ag}}{n_f}. \tag{8}$$

The distance of air bubbles within flux from the EFPI sensor or flux surface can be calculated, as the flux undergoes solidification. As shown in the Fig. 6, when reflector R_4 is formed, another cavity with reflectors (R_1, R_4) manifests. The light intensity reflected from this cavity is given as

$$R_c = R_1 + R_4 + 2\sqrt{R_1 R_4}\cos[\Delta\varphi_c + \varphi_0] \tag{9}$$

where R_c is the reflected light intensity, which can be obtained from FFT of modulated spectrum and φ_c is the phase difference due to the cavity length variation from reflector R_4. This cavity length l_c can be calculated by

$$\Delta\varphi_c = \frac{4\pi\,\Delta\left(n_g l_c\right)}{\lambda_m} \tag{10}$$

where l_c is the distance of the air bubble within flux from the EFPI sensor or mold wall, as shown in Fig. 6 and n_g is the group refractive index of air gap and the flux film. The time varying air gap, thickness of the flux and distance of air bubble within flux from the EFPI sensor can be measured in real time and example results are included in Section IV-A. The temperature dependent crosstalk for both air gap and flux thickness measurement can be expressed by the following equation:

$$\Delta(nl) = (nl)\alpha_c \Delta T \tag{11}$$

where α_c is the co-efficient of thermal expansion of silica $= 0.55e-6\ \text{C}^{\circ-1}$ *and* ΔT is the temperature during solidification.

III. Spectrum Acquisition and Data Processing

A. Data Acquisition and Processing

An interferogram is acquired by the Micrometer-Optics Hyperion SI-255 optical broadband interrogator. At each time interval, an interferogram of 20 000 points is obtained having a wavelength band of 1460–1620 nm. This spectrum was fed to an in-house developed low-finesse EFPI demodulation algorithm to estimate the air gap in real time. Data were acquired for 330 s (∼5 min) on average for two flux evaluations. FFT of the spectra was obtained from which multiple peaks were identified near the shorter and longer optical lengths. This indicates the presence of several trapped air bubbles within the flux separate from the air gap. The largest FFT peak after dc component corresponds to the air gap. The subsequent peaks next to the air gap peak correspond to the reflections from within the flux due to the trapped air bubbles. The dc component of the FFT signal is the dc offset (always real for a real signal) that pertains to the 0 μm optical path length. The right-most peak corresponds to the reflection from the opposite mold wall.

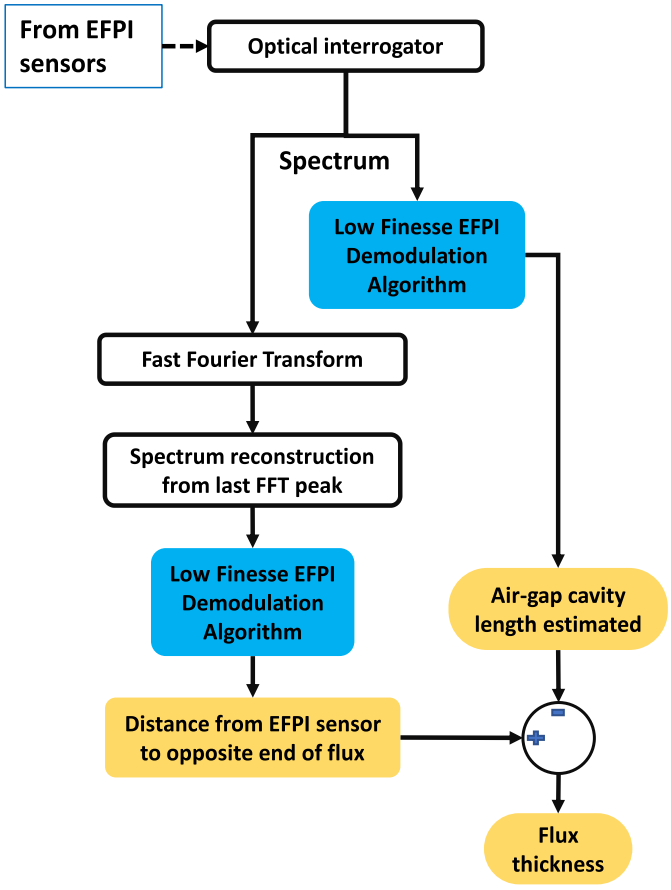

Fig. 7. Data acquisition and data processing flowchart for air gap and thickness measurements.

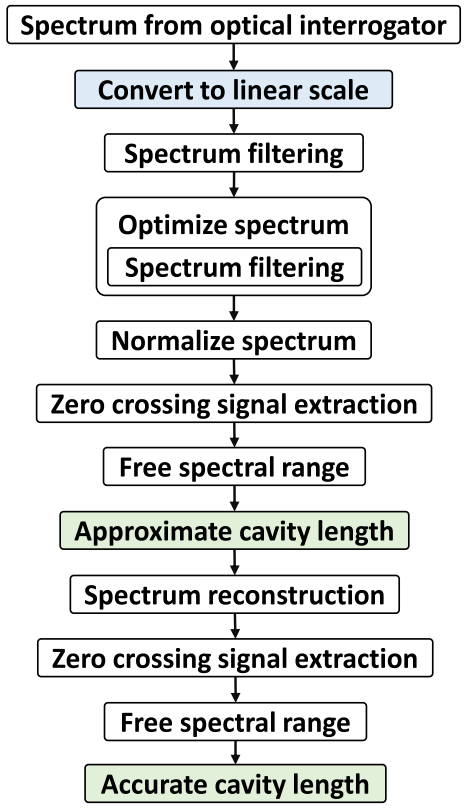

Fig. 8. Low-Finesse EFPI demodulation algorithm flowchart to determine air gap from the interferogram.

The spectrum is acquired by the optical interrogator, which is controlled by a data acquisition laptop. No additional filtering is used as the high-frequency components from the spectrum are required to obtain information from inside the flux sample. The spectrum is processed to obtain an FFT signal. The right-most peak in the FFT corresponding to the longest optical length is considered from which a new spectrum is constructed and processed with the EFPI demodulation algorithm. The distance from the EFPI sensor to the opposite end of the flux is measured and subtracting the air gap provides the thickness of the mold flux. The distance of trapped air bubbles within flux from EFPI sensor is measured in a similar fashion. The data acquisition and processing flow is shown in Fig. 7. It uses the in-house developed low-finesse EFPI demodulation algorithm to determine the air gap and thickness.

B. Low-Finesse EFPI Demodulation Algorithm

Using (2), (4), and (8), the respective cavity lengths can be estimated; however, directly doing so will result in very poor resolution for larger cavity lengths. This means that the effective measurement range of the EFPI system becomes less accurate. To extend this measurement range to larger distances, an advanced signal processing method involving zero crossing and spectrum reconstruction is used. The EFPI demodulation flowchart is included in Fig. 8. This algorithm can achieve cavity length that was measured with high resolution (∼1 nm) in the laboratory environment. This is possible only on an optical table and with a perfect external reflector such as a silicon wafer. But the algorithm performs reasonably well in an environment with disturbances and gives a reasonable resolution of 0.1 μm $\pm$ 10 nm when determining cavity length. This makes it quite suitable to measure the structural features of the mold flux in real time. The code for this algorithm was developed in the LabVIEW tool.

This sub-VI was used as a function call in the main real-time data acquisition program developed in LabVIEW. It takes in the interferogram at any time instant as an input argument and performs filtering and optimization with wavelet detrending. As shown in Fig. 8, the spectrum was normalized, and zero-crossing detection was performed. A two-step demodulation process with zero crossing signal analysis is performed and the spectrum is reconstructed for accurate determination of the air gap. For determining thickness, an algorithm was used to estimate the mold gap from the FFT spectra, which was subtracted from the air gap. This two-step demodulation process involved the computation of FSR values, which are used to calculate an approximate mean cavity length. Then this cavity length is inversely computed to obtain a singular FSR from which the interferogram is reconstructed. Zero-crossing detection was performed again on the reconstructed spectrum. This spectrum reconstruction eliminates the phase noise from the signal, yielding a constant FSR value from which accurate cavity length can be determined in real time.

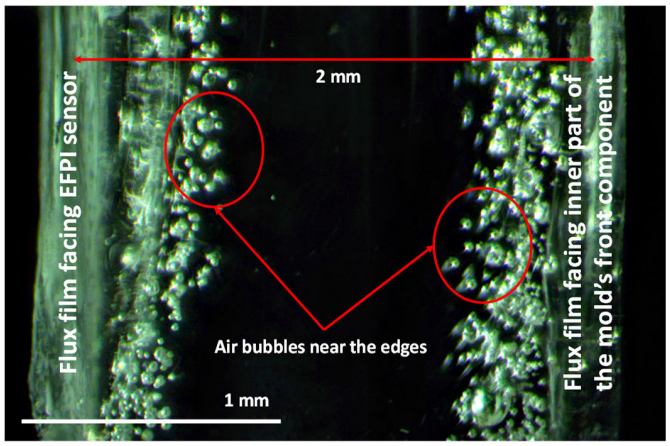

Fig. 9. Optical microscope image of H2-9 flux sample after solidification.

IV. Results and Discussions

Experiments were performed by pouring the molten flux at 1400 °C into the instrumented mold at room temperature. The point gap sensors installed in the mold measured the air gap between the mold wall and shrinking flux, as well as flux thickness due to the formation of an extrinsic EFPI. The formation of multiple reflectors in the EFPI, as shown in Fig. 6, gives a modulated interferogram that is captured by the EFPI sensors dynamically as the flux undergoes solidification. After the mold flux solidifies completely, a stable modulated interferogram is observed, which suggests that the flux film's air gap and thickness reaches a steady state fairly rapidly. The solidified flux sample is shown in Fig. 9, from which it can be observed that the flux sample is translucent. The coloring of the flux film sample after solidification is dependent on its basicity and composition [44], [45].

The flux sample in Fig. 9 is translucent in appearance due to the overall composition. The flux basicity can influence the amount of bubble formation. During solidification, the air bubbles get trapped within the flux near the mold edges, which results in the modulation of the interferogram.

A. Interferogram

Interferograms acquired from the three EFPIs installed in the mold are shown in Fig. 10(a) and (b) for both trials. The corresponding FFT spectra are shown in Fig. 10(c) for the near side and Fig. 10(d) for the far side of the mold. Each mold step where the mold flux solidifies has a different reflectivity. This is the reason for the changing fringe visibility in each step of the mold. Spectra recorded 2 min after the pour for each experimental trial are shown in Fig. 10, with the corresponding FFT signal. The measured spectra are modulated indicating multiple reflectors being formed in the flux.

Interferograms from each mold flux experiment are presented only for the bottom EFPI, as the optical interrogator's maximum measurement range is limited to 3.5 mm, which is exceeded by middle (4 mm) and top (6 mm) step EFPI sensors in the mold.

Before flux was poured into the mold gap, the bottom EFPI interferogram shown in Fig. 11(a) was acquired. The parabolic

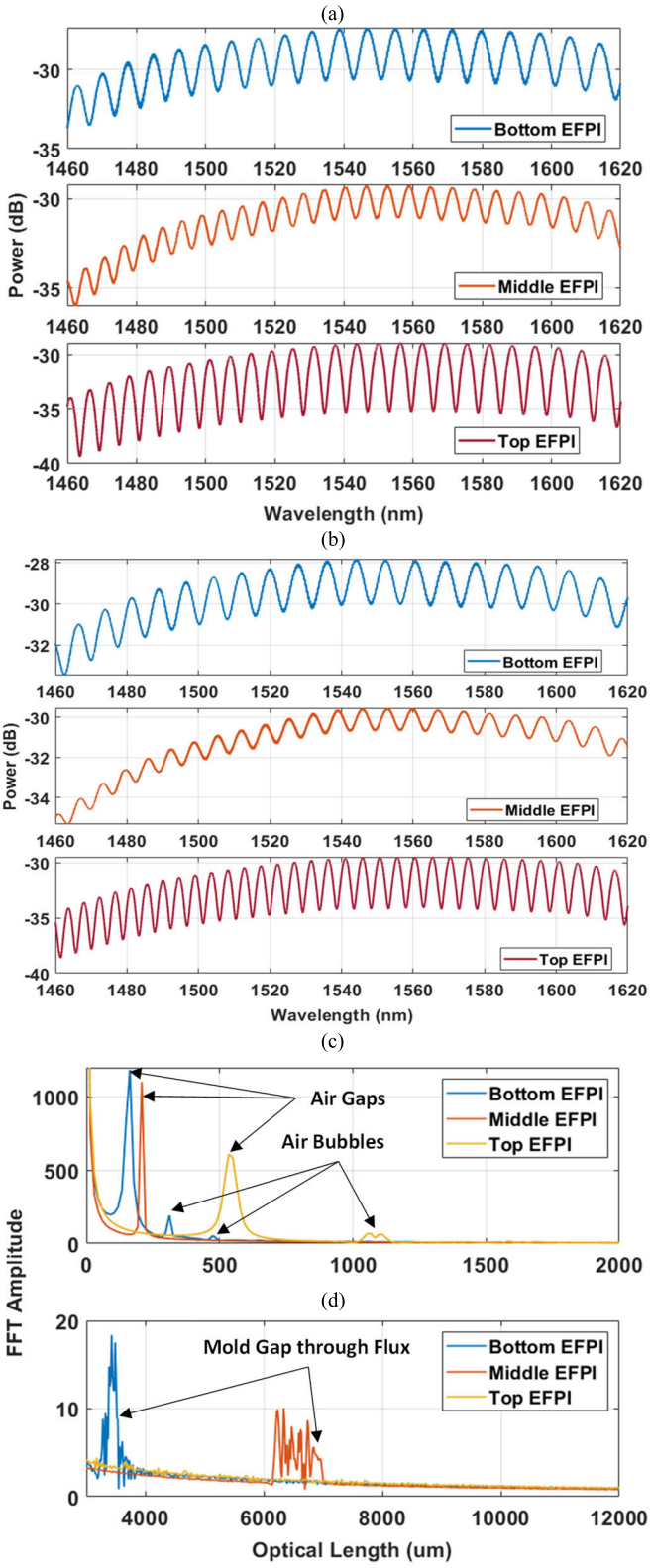

Fig. 10. Interferogram for solidification of mold flux samples. (a) Interferogram for H2-7 flux. (b) Interferogram for H2-9 flux. (c) FFT of flux film near EFPI side. (d) FFT of flux film opposite EFPI side.

trend of the full interferogram is due to the signature of the swept laser from the Hyperion SI-255 optical interrogator. The modulation of this spectrum is shown in Fig. 11(b)

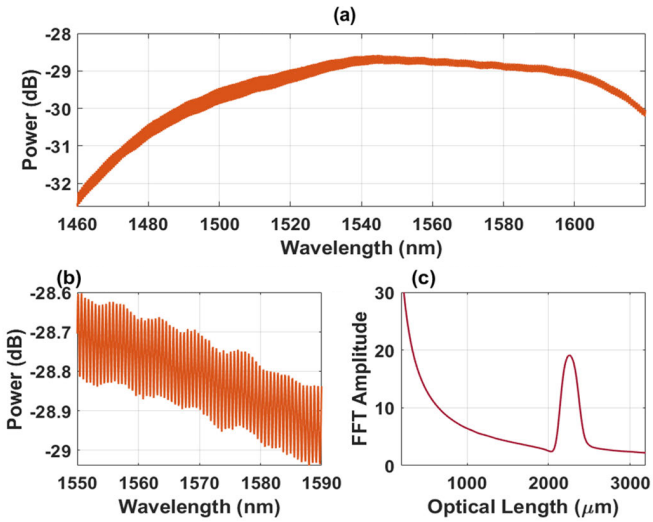

Fig. 11. Bottom EFPI spectrum before the molten flux was poured into the mold. (a) Spectrum before flux pour. (b) Spectrum between 1550 and 1590 nm. (c) FFT of the spectrum in (a), between 0 and 3500 μm.

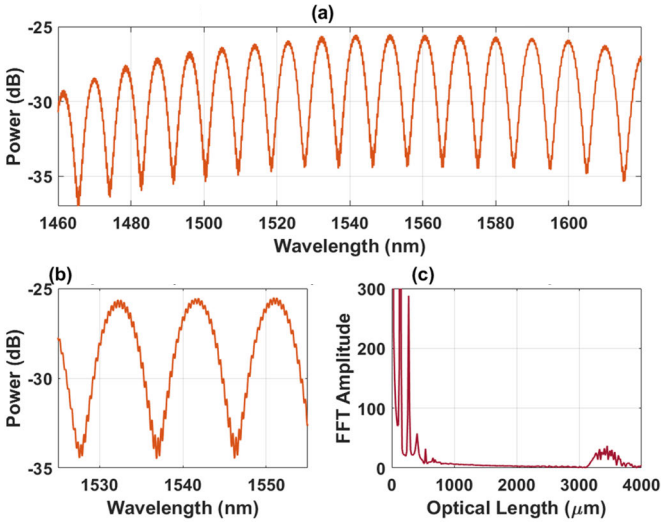

Fig. 12. Bottom EFPI spectrum at the instance when molten flux was poured into the mold. (a) Spectrum at time of flux pour. (b) Spectrum between 1525 and 1555 nm. (c) FFT of the spectrum in (a), between 0 and 4000 μm.

between wavelengths 1550 and 1590 nm for the reflection of light from the interior of the opposite wall of the mold. This interferogram yields a total mold gap measurement of ~2 mm for the bottom EFPI sensor. The FFT of this spectrum with respect to optical length in μm is shown in Fig. 11(c), which shows a peak after the dc component at 2130 μm. This matches the physical length of the mold gap. The changes observed in the measured spectra for the bottom EFPI during flux solidification and shrinkage will now be discussed.

When the flux sample is poured into the mold, the bottom EFPI acquired spectrum is, as shown in Fig. 12(a). This is due to the mold gap getting filled with the molten flux; however, the EFPI demodulation algorithm with its advanced signal processing capability, estimates the air gap accurately. In Fig. 12(b), the spectrum is expanded between wavelengths 1525 and 1555 nm. The spectrum appears modulated due to

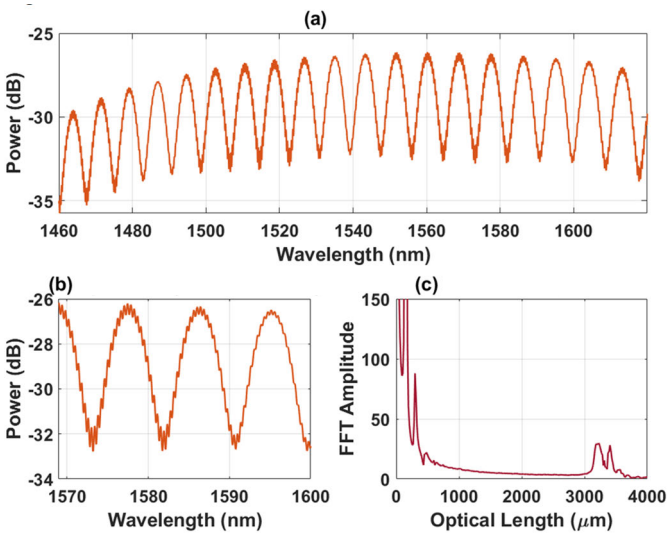

Fig. 13. Bottom EFPI spectrum acquired four seconds after molten flux was poured into the mold. (a) Spectrum during flux solidification. (b) Spectrum between 1569 and 1600 nm. (c) FFT of the spectrum in (a), between 0 and 4000 μm.

reflections from the interior of the flux film and the opposite mold wall. The FFT result for this spectrum is shown in Fig. 12(c). From this, it is observed that the air gap forms almost instantly. The short peak at 106.89 μm in the FFT signal corresponds to the air gap, which is formed due to the rapid pullaway of the flux film from the mold wall. The peak at 2130 μm observed in Fig. 11(c), moves away to ~3300 μm and becomes broader, as shown in Fig. 12(c). This is the optical path change due to the change in refractive index from air (~1) to flux (~1.52). The peak is broad because of the reflections from multiple air bubbles within the flux near the edge of the solidified flux.

The interferogram acquired 4 s after pouring the molten flux sample into the mold is shown in Fig. 13(a). The peak and valley regions of this spectrum appear to be thicker. From this, it can be inferred that the modulated spectrum has high-frequency components that vary slightly with time. This means that there are multiple reflectors being formed within the flux material. This is evident by observing the signal between 1569 and 1600 nm, as shown in Fig. 13(b). The interferogram was processed to obtain the FFT, as shown in Fig. 13(c). Multiple evolving peaks were observed in this FFT signal as the solidification progressed. The large peak at the right side of the dc component corresponds to the total air gap between the mold wall and mold flux sample undergoing solidification. Smaller peaks neighboring the air gap peak correspond to the reflection from the trapped air bubble at ~400 μm being formed within the flux material. The FFT signal between 3000 and 4000 μm consists of multiple peaks. The last peak toward the right side corresponds to the reflection from the interior of the front component of the mold wall and the remaining peaks are due to reflections from trapped air bubbles within the flux close to the edge.

The interferogram shown in Fig. 14(a) was acquired after the mold flux completely solidified. It appears thicker than the interferogram shown in Fig. 13(a). At this time, the flux

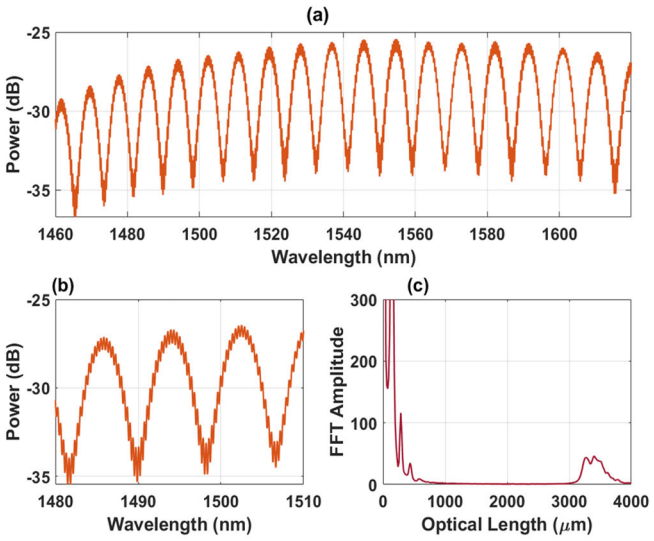

Fig. 14. Bottom EFPI spectrum acquired after solidification of molten mold flux in the mold. (a) Spectrum after flux shrinkage. (b) Spectrum between 1480 and 1510 nm. (c) FFT of the spectrum in (a), between 0 and 4000 μm.

TABLE II
MOLD FLUX COMPOSITION

Flux composition (wt. %)	H2-7	H2-9
CaO	0.29	0.30
SiO_2	0.27	0.29
MgO	0.04	0.04
Al_2O_3	0.13	0.10
Na_2O	0.15	0.15
F	0.09	0.09
Basicity	1.06	1.06

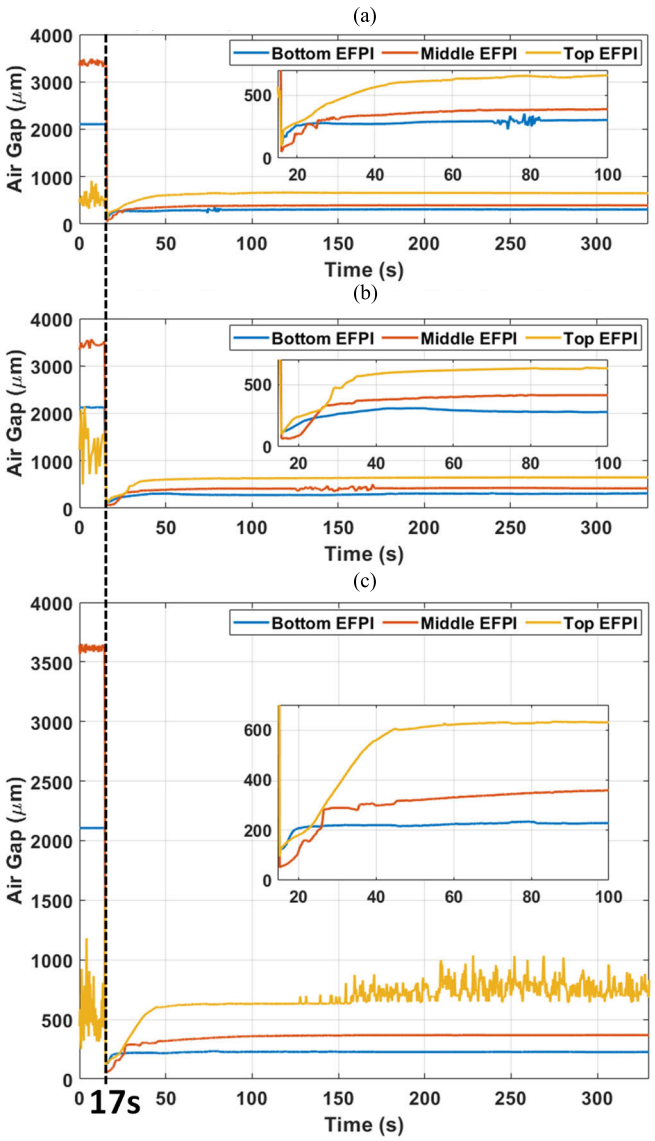

Fig. 15. Air gap or cavity length estimated in real time by the low-finesse EFPI demodulation algorithm. (a) H2-7 flux sample air gap trial-1. (b) H2-7 flux sample air gap trial-2. (c) H2-9 flux sample air gap.

film has cooled to the temperature of the mold and has undergone shrinkage. The spectrum remains stable after the solidification process. The high-frequency modulations in the spectrum shown in Fig. 14(b) expanded between wavelengths 1480 and 1510 nm remain stable and do not evolve further. From the FFT of the interferogram shown in Fig. 14(c), it can be observed that all the peaks after dc component have shifted slightly toward the right, i.e., increased in optical length. The peaks have also increased in terms of reflected power because of the transparency of the flux sample. The peaks observed in the FFT for the acquired interferogram are used to determine the thickness and location of trapped air bubbles as discussed in the measurement theory section.

Each flux material composition in (wt.%) ratio is given in this table along with basicity information in Table II. To get the modified basicity of H2-7, aluminum oxide content was varied and balanced with silica. For H2-9, silica was varied and balanced with calcium oxide maintaining constant aluminum oxide content. Molten flux samples are relatively viscous (0.5–0.4 Poise), which makes filling difficult in small gaps such as 2 mm. The viscosity of flux sample is reduced by increasing the basicity of the material. The basicity and composition of flux samples used in this experiment are included in Table II. The information in the table is in percentage weight ratio.

B. Air Gap Measurement

The air gap measurement is obtained directly by processing the interferogram using the low-finesse EFPI demodulation algorithm as it is a low-frequency signal demodulation. It ignores the higher frequencies in the case where the interferogram is modulated. The insets in Fig. 15 show the first 100 s of the air gap measurement, which involves the solidification process. Two trials of H2-7 flux solidification are reported to demonstrate measurement repeatability. Phenomena such as crack formation and propagation can be seen. Cracking is due to the release of internal stresses built up from the fast quenching of the molten mold flux.

The top and middle EFPI signal measurement is not very clear before the pour in each trial as the step profile's mold

TABLE III
AIR GAP AFTER FLUX SOLIDIFICATION

Air gap after solidification	H2-7 (trial-1)	H2-7 (trial-2)	H2-9
Top EFPI (µm)	650.12	649.72	686.19
Middle EFPI (µm)	394.62	418.80	368.49
Bottom EFPI (µm)	306.93	313.97	226.59

Fig. 16. Cracking observed during solidification of H2-9 flux film sample.

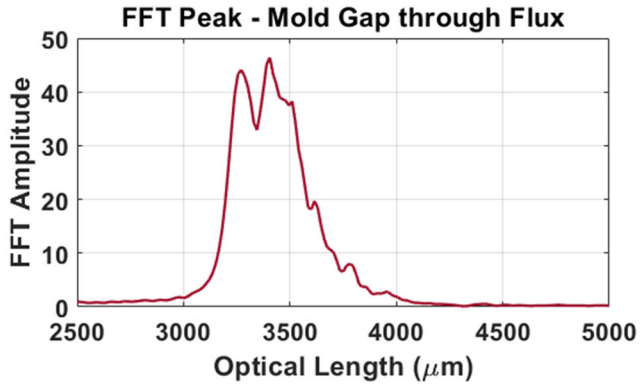

Fig. 17. FFT peak from which the spectrum is reconstructed for mold gap estimation through the flux medium.

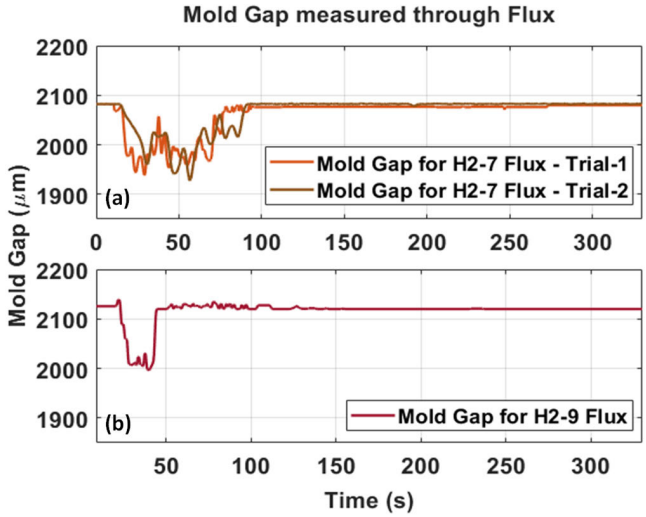

Fig. 18. Mold gaps measured for each flux sample during solidification. (a) Mold gap measured through H2-7 flux for two different trials. (b) Mold gap measured through H2-9 flux.

gap is 4 and 6 mm at these sensor locations. This is beyond the measurement capability of the optical interrogator, which is evident for the top EFPI in the FFT spectra shown in Fig. 10(d). Hence, only the bottom EFPI shall be considered for the thickness estimation. The air gaps are calculated according to (2) in the measurement theory section. The air gap plots shown in Fig. 15 have spikes at certain times, for example in Fig. 15(a) between 70 and 80 s. This is due to the cracking of mold flux film inside the mold due to stresses that develop during rapid cooling of the flux film. The air gap measurements gradually became stable after the molten flux started to solidify. Gap measurements ultimately reached the values shown in Table III. At the time of pouring, the cavity lengths measured are approximately equal to the internal offsets shown in Table I. As the flux samples solidify and shrink, the air gaps gradually reach the values shown here. When the mold flux basicity was high, slight temperature differences induced the cracking, which was observed in Fig. 15(c).

The cracking phenomenon of H2-9 flux was evident from 150 s of top EFPI's measurement. The cracks formed during solidification are shown in Fig. 16. The solidifying flux sample mechanically vibrates during crack formation, which leads to air gap measurements with a noisy appearance. The effects of cracking can be minimized by preheating the mold prior to conducting the experiment. This way the window of measurement can also be extended as the flux crystallization period is prolonged.

C. Thickness Measurement

For each spectrum acquired by interrogation of the EFPI sensor, the FFT signal was processed and the right-most peak was identified, as shown in Fig. 17 to determine the flux thickness. The sectioned FFT signal contains multiple peaks due to the reflections from several air bubbles at the far flux-mold wall boundary. The bottom EFPI-acquired interferogram is processed to obtain FFT and the right-most peak was selected for spectrum reconstruction, as shown in Fig. 17. Then, a low-finesse EFPI demodulation algorithm was used to estimate the optical length of the mold gap through each flux medium. This optical length was corrected with the appropriate refractive index to obtain the exact mold gap length (∼2 mm), as shown in Fig. 18. At certain times, the optical length of the mold may exceed the machined mold cavity since the RI is being assumed as a constant of 1.52.

The mold gap measurement for H2-7 flux for trial-1 shown in Fig. 18(a) varies as much as 120 μm up to 80 s, after which it remains stable. Between both trials of H2-7, there is a varia-

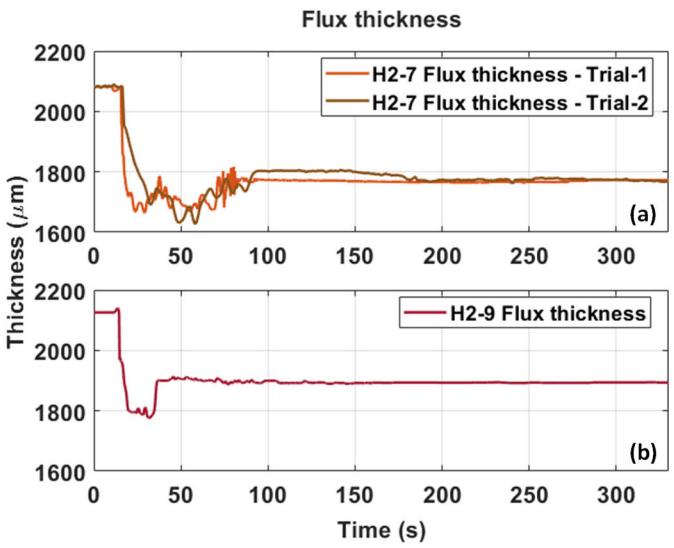

Fig. 19. Real-time thickness measurements of mold flux. (a) H2-7 real-time flux thickness for two different trials. (b) H2-9 real-time thickness.

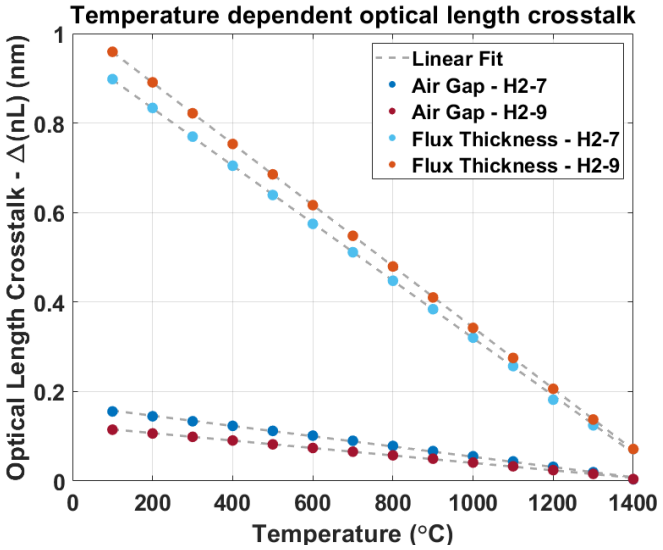

Fig. 20. Temperature-dependent optical path length crosstalk. Shows the interference of temperature on measured quantities.

tion of 2.58 μm, which is due to the mechanical irregularities of the mold. Similarly, the mold gap measurement for H2-9 flux shown in Fig. 18(b) varies as much as 100 μm up to 50 s, after which the variations reduce to $\sim$10 μm before becoming stable.

The thickness of the solidified mold flux film was measured by estimating the real-time difference between the air gap measurement by bottom EFPI shown in Fig. 15 and the mold gap estimates shown in Fig. 18 at each time instant of the experiment. These results were based on (8). The thickness measurements shown in Fig. 19 matched the postexperiment physical measurements after the difference was divided by an RI of 1.52. The flux thickness measurement remains consistently stable after 100 s in the case of H2-7 flux and 50 s in the case of H2-9 flux.

The thickness measurement indicates the total mold gap length ($\sim$2 mm) before the molten flux sample was poured into the mold. For the thickness measurement of H2-7 flux shown in Fig. 19(a), the flux thickness varies between 30 and 80 s due to the crack formation during the rapid quenching. The thickness measurement of H2-9 flux is shown in Fig. 19(b). It can be observed that thickness measurement reaches stability faster than H2-7 flux.

As the temperature decreases gradually during the solidification of the flux, the refractive index of the air gap and of the flux also gradually increases. This results in a marginal error with respect to the measured optical path lengths of the air gap and flux thickness. From the analysis in Fig. 20, the temperature-dependent cross-sensitivity can be determined as the slope of the linear fit for

1) air gap as -0.1147 nm/°C for H2-7 experiments and -0.0832 nm/°C for H2-9 experiment and
2) flux thickness as -0.6419 nm/°C for H2-7 and -0.6839 nm/°C for H2-9.

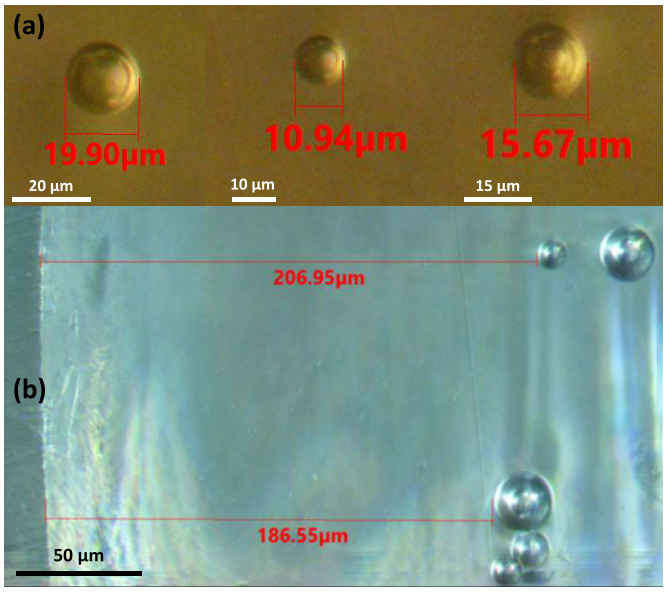

Fig. 21. H2-9 Flux sample with air bubbles in the EFPI path. (a) Trapped air bubbles in flux. (b) Distance of air bubbles from flux film edge facing the EFPI sensor.

D. Reflection From Air Bubbles Within the Flux

The proposed algorithm can also be used to locate the air bubbles being formed within the flux film sample. A few air bubbles get trapped and freeze directly in the path of the EFPI sensor-directed light, as shown in Fig. 21. After a portion of light gets reflected at the flux film's edge in the air gap, some light penetrates the flux film boundary and goes through the flux, where again some light gets reflected by the trapped air bubble within the flux. The air bubbles shown here are at 206.95 and 186.55 μm from the flux film boundary. Position with respect to time can be determined in real time with the EFPI sensor or mold wall as the reference. Considering the FFT transform of the interferogram, the second peak in Fig. 21 insert is detected and tracked using peak detection,

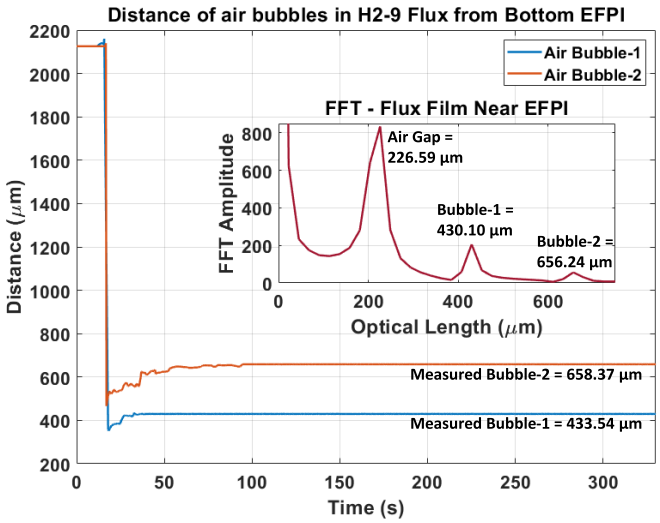

Fig. 22. Real-time FFT peak detection-based location measurement of the air bubbles in H2-9 mold flux from the EFPI sensor.

and the spectrum at this optical length is reconstructed. The low-finesse EFPI demodulation algorithm is used to estimate the distance from this reconstructed spectrum. This allows for real-time monitoring of the air bubble location, as shown in Fig. 22. This estimation is in accordance with (10). This method can be extended to measure the distances of multiple air bubbles within the flux during the solidification process depending on the number of peaks in the FFT signal. The variations in measurement are higher when the flux sample is still in the molten phase; however, as the flux sample solidifies, the air bubble gets trapped in place due to rapid quenching, resulting in a stable measurement.

The inset in Fig. 22 depicts the FFT of the interferogram during the solidification of the H2-9 flux. Two distinct peaks can be observed, where the large peak corresponds to the air gap and the small peak to its right corresponds to the reflection from the air bubble trapped within the flux. The measurement shown in Fig. 21 indicates an air bubble located at 430.10 and 656.24 μm from the EFPI sensor. The air bubbles manifest at different locations within the flux film; however, the time of air bubble formation is almost identical. This matches with the physical distance of the air bubble within the flux film from the EFPI sensor, shown in Fig. 21. For H2-9 flux sample, the air gap after flux shrinkage is 226.59 μm and the air bubble is located at 206.95 μm from the flux film boundary, as shown in Fig. 21(b). On adding these two values, one can obtain 433.54 μm, which is very close to the measured distance in Fig. 22. Similarly, the second air bubble is measured at a distance of 658.37 μm from the EFPI sensor.

V. Conclusion

In this research, a three-part stainless-steel mold with a three-step profile was designed and constructed and then successfully used for air gap and thickness measurements. Three EFPIs were instrumented successfully and installed in the center of each step profile of the mold such that they were flush with the mold wall. Mold flux samples were melted in a furnace and poured into the mold setup. The real-time interferogram was successfully acquired using a Hyperion SI255 optical interrogator. A low-finesse EFPI demodulation algorithm was developed to measure the air gap and thickness from the modulated interferogram in real time. Information regarding the presence of trapped air bubbles within the mold flux film was obtained from the modulated interferogram in real time. The proposed system of measurement can be applied in real-time monitoring of the shrinkage of molten metals as well. Several EFPIs in an array can be used to obtain high-resolution information regarding the surface properties of the materials at high temperatures. It can be challenging to distinguish between multiple fringes and determine the true value from the spectrum itself when the measurement target exceeds one cycle of the spectrum. The proposed system overcomes such issues by means of interferometry principles such as FFT, intercavity distance modification, and advanced signal processing. Further research is also being conducted to extend the measuring range of the designed EFPI sensor.

Acknowledgment

The author would like to thank Zoey Snyder from the Material Science Department for her assistance in polishing the flux film.

References

[1] K. C. Mills and A. B. Fox, "Mould fluxes," *High Temp. Mater. Processes*, vol. 22, nos. 5–6, pp. 291–302, Dec. 2003.

[2] X. Wang, H. Liu, M. Zhao, Q. Wang, X. Zhang, and S. He, "Effect of AlN on properties of non-reactive CaO-Al2O3-based mold flux for high-al steel," *Mater. Today Commun.*, vol. 34, Mar. 2023, Art. no. 105432.

[3] A. Yamauchi, K. Sorimachi, T. Sakuraya, and T. Fujii, "Heat transfer between mold and strand through mold flux film in continuous casting of steel," *ISIJ Int.*, vol. 33, no. 1, pp. 140–147, 1993.

[4] X. Deng et al., "Inclusion behaviour in aluminium-killed steel during continuous casting," *Ironmaking Steelmaking*, vol. 46, no. 6, pp. 522–528, Jul. 2019.

[5] C. A. M. Pinheiro, I. V. Samarasekera, J. K. Brimacomb, and B. N. Walker, "Mould heat transfer and continuously cast billet quality with mould flux lubrication part 1 mould heat transfer," *Ironmaking Steelmaking*, vol. 27, no. 1, pp. 37–54, Feb. 2000.

[6] A. W. Cramb, R. J. Fruehan, and A. S. Foundation, *The Making, Shaping and Treating of Steel: Casting*, AISE Steel Found. Three Gateway Center, Pittsburgh, PA, USA, 2003.

[7] E. I. Peterson, "Mold flux crystallization and mold thermal behavior," Dept. Mater. Sci. Eng., Missouri Univ. Sci. Technol., Rolla, MO, USA, 2017.

[8] T. J. Headley and R. E. Loehman, "Crystallization of a glass-ceramic by epitaxial growth," *J. Amer. Ceram. Soc.*, vol. 67, no. 9, pp. 620–625, Sep. 1984.

[9] F. C. Serbena, I. Mathias, C. E. Foerster, and E. D. Zanotto, "Crystallization toughening of a model glass-ceramic," *Acta Mater.*, vol. 86, pp. 216–228, Mar. 2015.

[10] G. Beall, "Design and properties of glass-ceramics," *Annu. Rev. Mater. Sci.*, vol. 22, no. 1, pp. 91–119, 1992.

[11] X. Wang, X. Yan, S. Luo, and C. Chen, "Flux growth of large KBBF crystals by localized spontaneous nucleation," *J. Cryst. Growth*, vol. 318, no. 1, pp. 610–612, Mar. 2011.

[12] J.-Y. Baek, S.-H. Shin, S.-H. Hyun, and J.-W. Cho, "Glass structure and crystallization via two distinct thermal histories: Melt crystallization and glass crystallization," *J. Eur. Ceram. Soc.*, vol. 41, no. 1, pp. 831–837, Jan. 2021.

[13] J. W. Cho and H. Shibata, "Effect of solidification of mold fluxes on the heat transfer in casting mold," *J. Non-Crystalline Solids*, vol. 282, no. 1, pp. 110–117, Apr. 2001.

[14] T. Pan et al., "Thermal shrinkage behavior of metal-organic frameworks," *Adv. Funct. Mater.*, vol. 30, no. 34, 2020, Art. no. 2001389.

[15] M. Brennan, J. Keist, and T. Palmer, *Defects in Metal Additive Manufacturing Processes*. Springer, 2021.

[16] A. Yamauchi, T. Emi, and S. Seetharaman, "A mathematical model for prediction of thickness of mould flux film in continuous casting mould," *ISIJ Int.*, vol. 42, no. 10, pp. 1084–1093, 2002.

[17] K.-W. Yi, Y.-T. Kim, and D.-Y. Kim, "A numerical simulation of the thickness of molten mold flux film in continuous casting," *Met. Mater. Int.*, vol. 13, no. 3, pp. 223–227, Jun. 2007.

[18] J. E. Shelby, *Introduction to Glass Science and Technology*. Alfred, NY, USA: Alfred Univ., Royal Society of Chemistry, 2020.

[19] W. Li et al., "Air gap measurement during steel-ingot casting and its effect on interfacial heat transfer," *Metall. Mater. Trans. B*, vol. 52, no. 4, pp. 2224–2238, Aug. 2021.

[20] A. Lagerstedt, J. Kron, F. Yosef, and H. Fredriksson, "Measurements and modeling of air gap formation in iron-base alloys," *Mater. Sci. Eng., A*, vols. 413–414, pp. 44–51, Dec. 2005.

[21] J. Majumdar, B. C. Raychaudhuri, and S. Dasgüpta, "An instrumentation scheme for multipoint measurement of mould-metal gap in an ingot casting system," *Int. J. Heat Mass Transf.*, vol. 24, no. 7, pp. 1089–1095, Jul. 1981.

[22] E. Vorathin, Z. M. Hafizi, N. Ismail, and M. Loman, "Review of high sensitivity fibre-optic pressure sensors for low pressure sensing," *Opt. Laser Technol.*, vol. 121, Jan. 2020, Art. no. 105841.

[23] V. Ahsani, F. Ahmed, M. Jun, and C. Bradley, "Tapered fiber-optic Mach–Zehnder interferometer for ultra-high sensitivity measurement of refractive index," *Sensors*, vol. 19, no. 7, p. 1652, Apr. 2019.

[24] E. Rodríguez-Schwendtner, M.-C. Navarrete, N. Díaz-Herrera, A. González-Cano, and Ó. Esteban, "Advanced plasmonic fiber-optic sensor for high sensitivity measurement of magnetic field," *IEEE Sensors J.*, vol. 19, no. 17, pp. 7355–7364, Sep. 2019.

[25] C. Zhu, Y. Zhuang, B. Zhang, R. Muhammad, P. P. Wang, and J. Huang, "A miniaturized optical fiber tip high-temperature sensor based on concave-shaped Fabry–Pérot cavity," *IEEE Photon. Technol. Lett.*, vol. 31, no. 1, pp. 35–38, Jan. 2019.

[26] S. Minakuchi et al., "Thermal strain in lightweight composite fiber-optic gyroscope for space application," *J. Lightw. Technol.*, vol. 33, no. 12, pp. 2658–2662, Jun. 15, 2015.

[27] C. M. Stiles, "A flexible fiber optic laryngoscope," *J. Amer. Med. Assoc.*, vol. 221, no. 11, pp. 1246–1247, Sep. 1972.

[28] L.-Y. Shao and J. Albert, "Compact fiber-optic vector inclinometer," *Opt. Lett.*, vol. 35, no. 7, pp. 1034–1036, 2010.

[29] D. Garcus, T. Gogolla, K. Krebber, and F. Schliep, "Brillouin optical-fiber frequency-domain analysis for distributed temperature and strain measurements," *J. Lightw. Technol.*, vol. 15, no. 4, pp. 654–662, Apr. 1997.

[30] A. Ukil, H. Braendle, and P. Krippner, "Distributed temperature sensing: Review of technology and applications," *IEEE Sensors J.*, vol. 12, no. 5, pp. 885–892, May 2012.

[31] C. Zhu et al., "A displacement sensor with centimeter dynamic range and submicrometer resolution based on an optical interferometer," *IEEE Sensors J.*, vol. 17, no. 17, pp. 5523–5528, Sep. 2017.

[32] H. Chen et al., "Fiber-optic, extrinsic Fabry–Pérot interferometric dual-cavity sensor interrogated by a dual-segment, low-coherence Fizeau interferometer for simultaneous measurements of pressure and temperature," *Opt. Exp.*, vol. 27, no. 26, pp. 38744–38758, 2019.

[33] J. Deng et al., "Optical fiber sensor-based detection of partial discharges in power transformers," *Opt. Laser Technol.*, vol. 33, no. 5, pp. 305–311, Jul. 2001.

[34] B. K. Nowakowski, D. T. Smith, and S. T. Smith, "Highly compact fiber Fabry–Pérot interferometer: A new instrument design," *Rev. Sci. Instrum.*, vol. 87, no. 11, pp. 115102-4–115102-8, Nov. 2016.

[35] Y. Du, Y. Chen, Y. Zhuang, C. Zhu, F. Tang, and J. Huang, "Probing nanostrain via a mechanically designed optical fiber interferometer," *IEEE Photon. Technol. Lett.*, vol. 29, no. 16, pp. 1348–1351, Aug. 2017.

[36] H. Xiao, J. Deng, G. Pickrell, R. G. May, and A. Wang, "Single-crystal sapphire fiber-based strain sensor for high-temperature applications," *J. Lightw. Technol.*, vol. 21, no. 10, pp. 2276–2283, Oct. 2003.

[37] K. L. Cooper, A. Wang, and G. R. Pickrell, "Optical fiber high temperature sensor instrumentation for energy intensive industries," Virginia Polytech. Inst. State Univ., Virginia Tech, Blacksburg, VA, USA, Tech. Rep. DOE/GO/11050429162, Tech. Rep., 2006.

[38] S. Ahn et al., "Fiber-optic temperature sensor based on cholesteric liquid crystals using 1250 nm band, >220 nm Wideband Wavelength-swept Laser," *Opt. Fiber Sensors*, 2022, Paper W4-67.

[39] G. H. Lee et al., "Output characterization of 220 nm broadband 1250 nm wavelength-swept laser for dynamic optical fiber sensors," *Sensors*, vol. 22, no. 22, p. 8867, Nov. 2022.

[40] S. Yamashita, Y. Nakazaki, R. Konishi, and O. Kusakari, "Wide and fast wavelength-swept fiber laser based on dispersion tuning for dynamic sensing," *J. Sensors*, vol. 2009, pp. 1–12, Sep. 2009.

[41] M. Njegovec and D. Donlagic, "Interrogation of FBGs and FBGs arrays using standard telecom DFB diode," *J. Lightw. Technol.*, vol. 34, no. 22, pp. 5340–5348, Nov. 2016.

[42] W. Ni et al., "Ultrathin graphene diaphragm-based extrinsic Fabry–Pérot interferometer for ultra-wideband fiber optic acoustic sensing," *Opt. Exp.*, vol. 26, no. 16, pp. 20758–20767, 2018.

[43] Z. Ran, Y. Rao, J. Zhang, Z. Liu, and B. Xu, "A miniature fiber-optic refractive-index sensor based on laser-machined Fabry–Pérot interferometer tip," *J. Lightw. Technol.*, vol. 27, no. 23, pp. 5426–5429, Dec. 2009.

[44] B. Zhang et al., "In situ and real-time mold flux analysis using a high-temperature fiber-optic Raman sensor for steel manufacturing applications," *J. Lightw. Technol.*, vol. 41, no. 13, pp. 4419–4429, Jul. 1, 2023.

[45] B. Zhang, H. Tekle, R. J. O'Malley, J. D. Smith, R. E. Gerald, and J. Huang, "In situ high-temperature Raman spectroscopy via a remote fiber-optic Raman probe," *IEEE Trans. Instrum. Meas.*, vol. 72, pp. 1–8, 2023.

Abhishek Prakash Hungund received the B.E. degree in electronics and communication from Visvesvaraya Technological University (VTU), Belagavi, Karnataka, India, in 2015, and the M.S. degree in electrical and computer engineering from the Lightwave Technology Laboratory, Missouri University of Science and Technology, Rolla, MO, USA, in 2023.

His research interests include the development of fiber optic-based interferometric sensors for air gap and thickness measurements of high-temperature substances, targeting continuous casting steel industries for quality improvement, and process optimization. His current research interests include fiber optic sensors and microwave interferometry for atomic and molecular sensing in high-temperature conditions.

Hanok Tekle received the B.S. degree in metallurgical engineering from the Missouri University of Science and Technology, Rolla, MO, USA, in 2020, where he is currently pursuing the Ph.D. degree in material science.

His current research interests include applied distributed fiber optic sensors in steelmaking and high-temperature Raman spectroscopy work with slag systems.

Bohong Zhang (Member, IEEE) received the Ph.D. degree in electrical engineering from the Missouri University of Science and Technology, Rolla, MO, USA, in 2022.

He is currently an Assistant Research Professor with the Lightwave Technology Laboratory, Department of Electrical and Computer Engineering, Missouri University of Science and Technology. His current research interests include center around the advancement of optical and microwave sensors and instrumentation, focusing on their applications in intelligent infrastructures, biomedical sensing, and challenging environments.

Dr. Zhang is a member of SPIE and OSA and an Associate for Iron and Steel Technology (AIST) Organization.

Ronald J. O'Malley is currently the F. Kenneth Iverson Chair Professor of steelmaking technologies with the Department of Metallurgical Engineering, Missouri University of Science and Technology, Rolla, MO, USA. He is also the Director of the Kent D. Peaslee Steel Manufacturing Research Center (PSMRC), which is an industry-supported consortium with 19 industry members that support∼US $1M in research annually. He is also the PI for > US $18M in research with the Department of Energy (DOE) and the Defense Logistics Agency (DLA) in areas of sensor development, hydrogen steelmaking, and electric furnace optimization. He has more than 30 years of experience in the metals manufacturing industry at Alcoa, Alcoa Center, PA, USA; Armco/AK Steel, Middletown, OH, USA; and Nucor Steel, LLC, Decatur, AL, USA. He has authored more than 150 journal and conference proceedings papers, over 70 invited and contributed presentations, and holds three US patents. He is a Lecturer for several short courses in steel manufacturing, including the Brimacombe short course on Continuous Casting. His current research interests include H2 ironmaking, EAF steelmaking, steel refining, clean steel processing and inclusion engineering, steel-refractory interactions, continuous casting, deformation processing, sensor development for harsh steelmaking environments, and new steel grade development.

Dr. O'Malley was the President of the Association for Iron and Steel Technology (AIST) from 2019 to 2021. He is an AIST Distinguished Member and a fellow.

Jeffrey D. Smith is currently a Professor of ceramic engineering with the Department of Materials Science and Engineering, Missouri University of Science and Technology, Rolla, MO, USA. His current research interests include high-temperature inorganic chemistry, materials characterization, high-temperature materials, and interactions between ceramics and molten materials.

Rex E. Gerald, II received the B.A. degree (Hons.) in chemistry from The University of Chicago (UC), Chicago, IL, USA, in 1984, and a conjoint Ph.D. degree in physical chemistry from the University of Illinois Chicago (UIC), Chicago, and the Max Planck Institute (MPI), Heidelberg, Germany, in 1994.

He is currently a Research Professor with the Lightwave Technology Laboratory, Department of Electrical and Computer Engineering, Missouri University of Science and Technology (MS&T), Rolla, MO, USA. He holds 26 US patents and coauthored more than 80 publications from research investigations conducted at UC; UIC; MPI; Argonne National Laboratory, Lemont, IL, USA; and MS&T.

Jie Huang (Senior Member, IEEE) received the Ph.D. degree in electrical engineering from Clemson University, Clemson, SC, USA, in 2015.

He is currently the Roy A. Wilkens Endowed Associate Professor of electrical and computer engineering with the Missouri University of Science and Technology, Rolla, MO, USA. He has established the Lightwave Technology Laboratory (LTL), Rolla, with a strong track record of sustained research funding, high-quality journal publications, and state-of-the-art research infrastructures with cutting-edge capabilities. He has authored or coauthored over 100 refereed articles, 70 conference papers, one book chapter, and ten US patent applications, all in the arena of advanced sensors. His current research interests include the development of optical and microwave sensors and instrumentation for applications in energy, intelligent infrastructures, clean environments, biomedical sensing, and harsh environments.